Broadband Tamm plasmon polariton

Andrey M. Vyunishev,[1,2] Rashid G. Bikbaev,[1,2,*] Sergey E. Svyakhovskiy,[3] Ivan V. Timofeev,[1,2] Pavel S. Pankin,[1,2] Stanislav A. Evlashin,[4] Stepan Ya. Vetrov,[1,2] Sergey A. Myslivets,[1,2] and Vasily G. Arkhipkin[1,2]

[1]*Kirensky Institute of Physics, Federal Research Center KSC SB RAS, Krasnoyarsk 660036, Russia*
[2]*Siberian Federal University, Krasnoyarsk 660041, Russia*
[3]*Department of Physics, M.V. Lomonosov Moscow State University, Moscow 119991, Russia*
[4]*Center for Design, Manufacturing and Materials, Skolkovo Institute of Science and Technology, 3 Nobel Street, Moscow 143026, Russia*
Corresponding author: bikbaev@iph.krasn.ru

A broadband Tamm plasmon polariton localized at the interface between the Bragg mirror and a thin metallic layer has been theoretically and experimentally investigated. The possibility of a localized state formation has been demonstrated and energy coefficients at the Tamm plasmon polariton wavelength have been predicted in the framework of the coupled mode theory. The metallic layer material and thickness corresponding to the maximum coupling between the incident radiation and the Tamm plasmon polariton has been determined. Experimental reflectance and transmittance spectra of the structure consisting of the Bragg mirror and chromium layers of different thicknesses have been measured. The analysis of the energy spectra shows the existence of the wavelength range with the near-unity absorption coefficient inside the Bragg mirror bandgap. The use of chromium as a metal results in the broadband Tamm plasmon polariton excitation. It is demonstrated that the experimental data is in a good agreement with the calculation.   © 2019 Optical Society of America

https://doi.org/10.1364/JOSAB.36.002299

1. INTRODUCTION

In recent years, a special type of a surface standing wave known as Tamm plasmon polariton (TPP) has been intensively investigated. Such a state is formed at the interface between a Bragg mirror (BM) and a conducting medium with $\varepsilon < 0$ [1] and is an optical analog of Tamm electronic states from solid-state physics [2]. The TPP can be experimentally observed as a narrow peak in the transmission, refraction, and absorption energy spectra of a structure [3,4].

Not only metallic layers, but also metal–dielectric nanocomposites can be used as negative permittivity materials with the resonant dispersion $\varepsilon < 0$. In particular, in [5] the possibility of TPP formation at the interface between the BM and a nanocomposite representing a transparent matrix with uniformly dispersed silver nanoparticles was demonstrated for the first time. The formation of the TPP in the case of BM conjugation with a layer of strongly anisotropic nanocomposite is studied in [6]. In [7], a mechanism of formation of two TPPs at the interface between the superlattice and a nanocomposite consisting of spherical nanoparticles with the dielectric core and metallic shell was proposed. The possibility of TPP formation in porous and gyroidal plasmonic materials was discussed in [8,9]. Later in [10–12], the possibility of the TPP localization at the interface between a BM and an epsilon near-zero nanocomposite was shown.

The TPP properties opened the opportunity of using these states for designing new devices, including absorbers [13–16], switches [17], organic solar cells [18], thermal emitters [19], sensors [20,21], and control of spontaneous emission [22]. The amplification of the local intensity of the field by means of excitation of TPP can be used in nonlinear optics problems studied in [23–26]. Hybridization of TPP with other types of localized modes can be used in lasers [27,28], single-phonon sources [29], and for electro-optical tuning of Tamm plasmon exciton polaritons [30]. Zhang *et al.* [31] experimentally demonstrated a white organic light-emitting diode based on the hybrid state formed by the interaction of the TPP and a microcavity mode. The white light is obtained via overlapping the visible spectral range by the hybrid state. Thus, such a device can only be created under interaction of broadband modes. In this case, the TPP spectral line can be broadened by choosing the parameters of a structure [31] or a metallic layer material [32]. In this study, we demonstrate the formation of broadband TPPs localized at the BM/thin metallic layer interface and investigate the dependence of the TPP wavelength on thicknesses of the metallic layer and first BM layer. We demonstrate that absorption at the TPP wavelength attains 95%, which allows the proposed model to be used as a broadband absorber.

2. RESULTS AND DISCUSSION

A. Theoretical Model

The model considered in this study is a one-dimensional multi-layer structure composed of a finite dielectric distributed Bragg mirror covered by a thin metallic layer of thickness d_m (Fig. 1). The BM unit cell is formed of two types of alternating dielectric layers with high (H) and low (L) refractive indices n_H, n_L and thicknesses d_H, d_L, respectively. The one-unit cell on the top of the BM can be truncated continuously to provide smooth transition from HLH… to HLH… configuration. Below, we assume the BM to be placed in air environment with refractive index $n_{air} = 1$.

For certainty, we investigate porous quartz (SiO_2) with refractive indices of $n_L = 1.22$ and $n_H = 1.45$ as a BM material. The layer thicknesses are $d_L = 150$ nm and $d_H = 127$ nm, respectively. The number of layers is $N = 101$.

We investigate a TPP localized at the interface between the BM and thin metallic layer. This localized state has a finite quality factor so the energy of the TPP can dissipate with amplitude relaxation rate γ. Three possible channels of a dissipation of energy can be considered: the transmission through the Bragg mirror, the transmission through the metallic layer, and the dissipation within the metallic layer. The relaxation rates can be denoted as γ_{bm}, γ_m, and γ_d, respectively, which are equal to the ratios of leakage power and the energy stored in the TPP. Therefore, the relative values of the relaxation rates are proportional to the power of relaxation in each channel and can be simplified as [19]

$$\gamma_m:\gamma_d:\gamma_{bm} = T_m:A_m:T_{bm}, \tag{1}$$

where T_m and T_{bm} are the transmittance of the metal layer and the BM, respectively, and A_m is the absorption coefficient of the metal layer.

According to the temporal coupled mode theory [33–35], the reflectance, absorptance, and transmittance of the structure are determined using the expressions

$$R(\omega) = \frac{|s_{1-}|^2}{|s_{1+}|^2} = \frac{(\omega - \omega_0)^2 + (\gamma_m - \gamma_d - \gamma_{bm})^2}{(\omega - \omega_0)^2 + (\gamma_m + \gamma_d + \gamma_{bm})^2}, \tag{2}$$
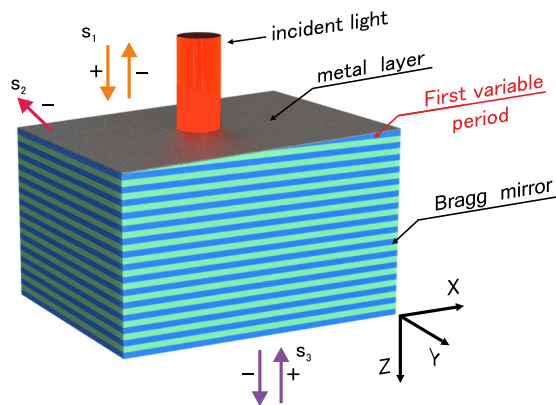

Fig. 1. Schematic of the structure consisting of a Bragg mirror and a thin metallic layer. $|s_{1+,-}|^2$ and $|s_{3+,-}|^2$ are the leakage powers in transmission and reflection channels of the structure, respectively, $|s_{2-}|^2$ is the leakage power in the absorption channel of the metallic layer.

$$A(\omega) = \frac{|s_{2-}|^2}{|s_{1+}|^2} = \frac{4\gamma_m\gamma_d}{(\omega - \omega_0)^2 + (\gamma_m + \gamma_d + \gamma_{bm})^2}, \tag{3}$$

$$T(\omega) = \frac{|s_{3-}|^2}{|s_{1+}|^2} = \frac{4\gamma_m\gamma_{bm}}{(\omega - \omega_0)^2 + (\gamma_m + \gamma_d + \gamma_{bm})^2}, \tag{4}$$

where ω_0 is the TPP frequency, ω is the incident wave frequency, and $|s_{i+}|^2$ and $|s_{i-}|^2$ are the normalized leakage powers in the channels (Fig. 1). Let us consider the incident wave irradiates the metallic side of the structure. In case of the resonant TPP excitation ($\omega = \omega_0$) the relaxation via the radiation through the BM vanishes: the light passing is prohibited by the photonic bandgap. Hence $T_{bm} = 0$ and $\gamma_{bm} = 0$.

The critical coupling conditions has the form

$$\gamma_{bm} = 0; \qquad \gamma_m = \gamma_d \Leftrightarrow T_{bm} = 0; \qquad T_m = A_m. \tag{5}$$

The equality of the relaxation rates of the first and second channel leads to the full absorption of the radiation incident onto the metallic layer ($T = 0, R = 0, A = 1$ [Eqs. (2)–(4)]) by the structure.

For the metal layer at the resonance wavelength, its transmittance and absorptance depend on the thickness. This means that the energy relaxation rates in the excitation scheme through the metal Eq. (5) are connected parametrically through the thickness of the metal layer:

$$A_m(T_m) \neq \text{const.} \tag{6}$$

The critical coupling conditions can be found graphically. To qualitatively estimate the transmittance, reflectance, and absorptance of the metallic layer, we use the theory of stratified conducting media [36]. We consider a plane-parallel metallic layer with the refractive index $n_2 = \Re n + i\Im n$, which is placed between two dielectric media with refractive indices $n_1 = n_L$ and $n_3 = 1$. According to the Fresnel formula for light incident normally onto the interface between media 1 and 2, the amplitude of the reflected and transmitted wave is

$$r_{12} = \frac{n_1 - n_2}{n_1 + n_2}, \qquad t_{12} = \frac{2n_1}{n_1 + n_2}. \tag{7}$$

The expression for the amplitude at the interface between media 2 and 3 is determined the same way and the resulting amplitude of the wave reflected and transmitted from the metallic layer can be written as

$$r_m = \frac{r_{12} + r_{23}e^{2i\beta}}{1 + r_{12}r_{23}e^{2i\beta}}, \qquad t_m = \frac{t_{12}t_{23}e^{2i\beta}}{1 + r_{12}r_{23}e^{2i\beta}},$$

$$\beta = \frac{2\pi}{\lambda_0}n_2 h_m, \tag{8}$$

where λ_0 is the wavelength and h_m is the metallic layer thickness. In this case the reflectance, transmittance, and absorptance of the metallic layer are determined as

$$R_m = |r_m|^2, \qquad T_m = \frac{n_3|t_m|^2}{n_1}, \qquad A_m = 1 - R_m - T_m. \tag{9}$$

Refractive indices of Ag [37], W [38], Mo [38], Zn [39], Al [40], Ti [39], V [39], and Cr [41] were determined at a wavelength of 734.3 nm, which corresponds to the center of the
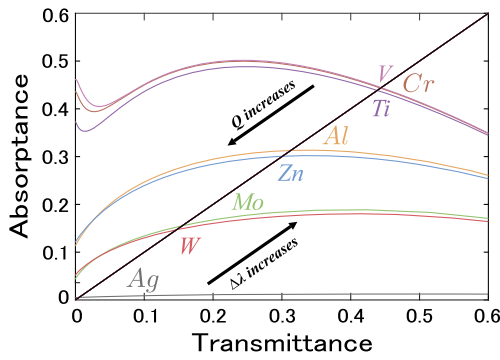
Fig. 2. Dependence of absorptance of the metallic film on its transmittance for different film materials. The $A_m(T_m)$ curves are across the critical coupling condition curve (black line). The cross points represent the critical coupling conditions for TPP resonance for different materials of the metal layer. The wavelength is $\lambda = 734.3$ nm.
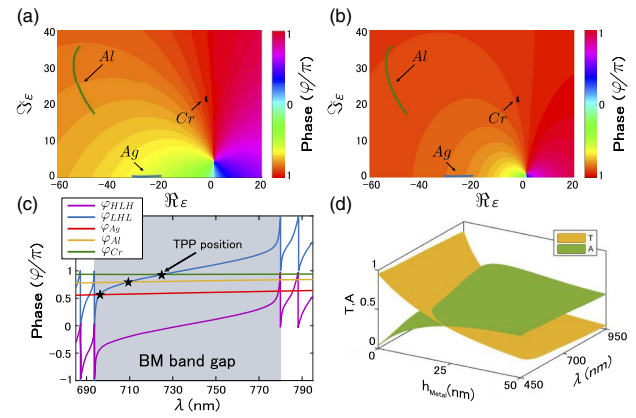

Fig. 3. Dependence of the reflected wave phase on the real and imaginary parts of the metallic layer permittivity at thicknesses of (a) 50 and (b) 10 nm at the wavelength corresponding to the BM bandgap center ($\lambda = 734.3$ nm). The regions with the constant phase of reflection from the metallic layer are shown by the continuous-tone filling. Lines show the phases of reflection from silver, aluminum, and chromium for wavelengths inside the BM bandgap. (c) Plot of phase matching condition Eq. (11) at a metallic layer thickness of $d_m = 10$ nm. (d) Transmission and absorption spectra of the chromium layer of different thicknesses.

bandgap of the BM. It can be seen from Fig. 2 that in the scheme of TPP excitation through the Ag layer, the critical coupling conditions [Eq. (5)] are established at lower transmittances and absorptances, i.e., at lower energy relaxation rates, the sum of which determines the resonance spectral linewidth.

It also can be seen from the figure that when the BM conjugate with W, Zn, Al, and Mo films, the critical coupling conditions are achieved at high transmittance and absorptance values. As a result, the spectral linewidth corresponding to the TPP increases [32]. The maximum width of the spectral line of TPP is achieved when the BM is conjugated with films of V, Cr, and Ti. In this case, a broadband TPP is localized at the interface between the BM and the metal film.

Thus, the coupled mode theory can predict the energy coefficients at the TPP frequencies and the width of the spectral line.

The TPP position will be determined by the phase matching condition [1]:

$$|r_\mathrm{m}|e^{i\varphi_\mathrm{m}}|r_\mathrm{bm}|e^{i\varphi_\mathrm{bm}} = 1, \tag{10}$$

where φ_m, r_m and φ_bm, r_bm are the phases and amplitudes of waves reflected from the metallic layer and BM, respectively. This is equivalent to the conditions for amplitudes,

$$|r_\mathrm{m}||r_\mathrm{bm}| = 1,$$

and phases,

$$\varphi_\mathrm{m} + \varphi_\mathrm{bm} = 2\pi n, \tag{11}$$

where $n = 0, 1, 2 \ldots$.

The phase of reflection from the metallic layer is defined as the argument of the complex reflection amplitude $\varphi_\mathrm{m} = \arg(r_m) = \arctan \Im(r_m)/\Re(r_m)$. Then, the φ_m value depends on the dielectric permittivity $\varepsilon = \Re\varepsilon + i\Im\varepsilon$ and the thickness of the metal layer. The Cole–Cole diagram method [42] is convenient to visualize the φ_m value. It can be plotted in coordinates of the real and imaginary parts of dielectric permittivity [Figs. 3(a) and 3(b)]. The phase φ_m was calculated in ranges of –60 to 20 for $\Re\varepsilon$ and of 0 to 40 for $\Im\varepsilon$ for thicknesses of metal of 10 and 50 nm.

It can be seen from Figs. 3(a) and 3(b) that the decrease in the metallic layer thickness from 50 to 10 nm strongly changes the phase of the reflected wave. In particular, the phase variations for silver, aluminum, and chromium are $\Delta\varphi_{\mathrm{Ag}} \approx 40°$, $\Delta\varphi_{\mathrm{Al}} \approx 20°$, and $\Delta\varphi_{\mathrm{Cr}} \approx 4°$, respectively. Thus, the TPP wavelength variation upon variation in the metallic layer thickness will be minimum when chromium is used.

To determine the phase $\varphi_\mathrm{bm} = \arg(r_\mathrm{bm})$ of reflection from a multilayer structure, we write the amplitude of reflection coefficient [43]:

$$r_{bm} = \frac{CU_{N-1}}{AU_{N-1} - U_{N-2}}, \tag{12}$$

where $U_N = \sin[(N+1)K\Lambda]/\sin[K\Lambda]$ and $K = (1/\Lambda)\arccos[(A+D)/2]$ is the Bloch wavenumber, N is the number of periods, $\Lambda = d_H + d_L$, A, B, C, and D are the elements of the 2 × 2 matrix, which relates the amplitudes of plane waves in layer 1 of the unit cell to the analogous amplitudes for the equivalent layer in the next BM unit cell [43].

The phase matching condition [Eq. (11)] and, consequently, the TPP formation, will be implemented at the points of intersection of the curves corresponding to the phase variation upon reflection from the BM and metallic layer $\varphi_\mathrm{m} = 2\pi - \varphi_\mathrm{bm}$ [Fig. 3(c)]. It can be seen that inside the BM bandgap the phase matching condition is fulfilled for the aluminum and chromium layers only in the case of the LHL BM configuration. It should be noted that the TPP position in the case of chromium nearly coincides with the bandgap center. In the case of a silver layer deposited onto the LHL structure, the TPP merges with the short-wavelength BM edge mode. The shift of the localized state wavelength toward the bandgap center becomes possible only at the additional reflected wave phase incursion. This can be obtained by changing the BM fist layer

thickness. Then, the phase matching condition takes the form

$$\varphi_{\mathrm{m}} + \varphi_{\mathrm{bm}} + \varphi_{\mathrm{first}} = 2\pi n. \tag{13}$$

The possibility of TPP formation upon variation in the BM first layer thickness is considered in more detail in the next section. The analysis of phase diagrams showed that to form a broadband TPP in a specified structure, it is reasonable to use chromium as a metallic layer material. Let us determine at which chromium layer thicknesses the condition for the critical coupling of the incident light with the TPP is valid.

Using Eqs. (7)–(9), we solve critical coupling conditions [Eq. (5)] graphically. To do this, we superpose the energy transmittance and absorptance spectra of the chromium layer depending on its thickness and the incident radiation wavelength [Fig. 3(d)]. The critical coupling is shown by the line of intersection of the absorptance and transmittance surfaces. This method allows us to build structures with the required parameters ensuring the critical coupling of the TPP with the incident light. It can be seen in Fig. 3(d) that the critical coupling corresponds to the relatively high transmittance and absorptance ($T \approx 0.5$, $A \approx 0.5$), which alters relaxation rates [Eq. (1)]. This allows us to obtain a broadband state, since the sum of relaxation rates determines the resonance contour width [Eqs. (2)–(4)]. The numerical calculation shows that critical coupling conditions [Eq. (5)] are valid at chromium layer thicknesses of about 6 nm. Deposition of such a thin metallic layer onto the BM will lead to the formation of a broadband TPP, at the wavelength of which the radiation will be completely absorbed by the structure in accordance with the above-described theory.

B. Numerical Calculation of Optical Properties of the Structure

To confirm the above-described theory, we calculated the transmission of a plane light wave propagating in the z direction (Fig. 1). To do this, we used the transfer matrix method [44].

The reflectance spectra of the BM combined with the chromium layer at different thicknesses of the layer adjacent to the metal are presented in Fig. 4.

It is worth noting that at the HLH configuration the reflectance inside the bandgap is maximum. In this case, condition [Eq. (11)] is not fulfilled and the TPP does not form. A smooth decrease in the H layer thickness leads to the additional phase incursion of incident wave [Eq. (13)], shift of the reflectance maximum to the short-wavelength bandgap edge, and TPP
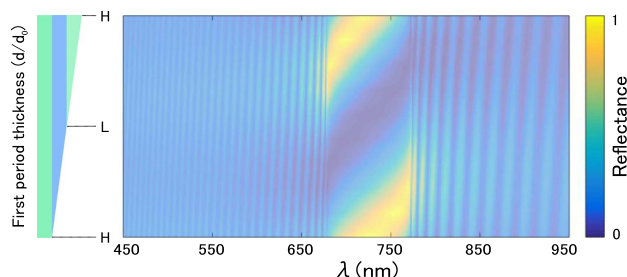
Fig. 4. Dependence of the reflectance spectrum of the structure on the thickness of the first period at the smooth transition from the HLH to LHL configuration and back with deposited Cr layer $d_{\mathrm{Cr}} = 6$ nm.
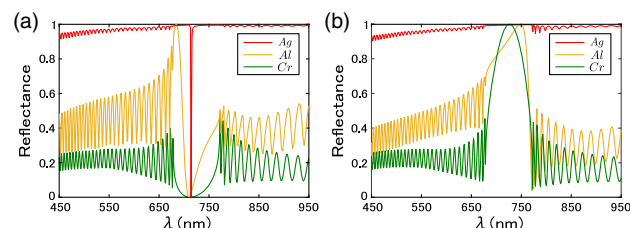
Fig. 5. Reflectance spectra of (a) the LHL and (b) HLH structures with the silver ($d_{\mathrm{Ag}} = 50$ nm), aluminum ($d_{\mathrm{Al}} = 5$ nm), and chromium ($d_{\mathrm{Cr}} = 6$ nm).

formation at its long-wavelength boundary. When the thickness d_{H} takes the zero value, the Bragg reflector begins with the layer with the low refractive index. In this case, the reflection is minimum inside the BM bandgap. This indicates the critical coupling of the incident radiation with the TPP [Eq. (5)] and validity of the phase matching condition [Eq. (11)].

The calculated reflectance spectra for the HLH and LHL configurations for different metallic layer materials are shown in Fig. 5. The layer thicknesses are fixed so that critical coupling conditions [Eq. (5)] are valid. The validity of the phase matching condition [Eq. (13)] for the deposited silver and aluminum layers is obtained by selecting the BM first layer thickness ($d_{\mathrm{first_{Ag}}} = 270$ nm, $d_{\mathrm{first_{Al}}} = 240$ nm). Then, the TPP wavelength will coincide with the bandgap center. According to the numerical calculation of the reflectance spectra, the use of aluminum and silver as metallic layer materials deposited onto the LHL configuration of the structure [Fig. 5(a)], leads to an increase in the TPP quality factor (Q) factor, which is observed as the resonance curve narrowing. When the critical coupling condition is valid, for the chromium layer deposited onto the BM, the TPP makes it possible to completely suppress reflection and maximize absorption.

Thus, the calculated data are in good agreement with the analytical results [Fig. 3(c)].

C. Measured Energy Characteristics of the Structure

The Bragg mirror layers with the above-described characteristics are formed by electrochemical etching of single-crystal silicon wafers in the ethanol solution of hydrofluoric acid (HF) with different concentrations (from 5% to 37%) [45]. The HF concentration in the electrolyte solution is checked by titration.

A silicon wafer, which serves as an anode, was placed into a polytetrafluoroethylene electrochemical cell. The silicon wafer backside is tightly pressed against the copper plate and the front side is in the electrolyte solution. The working surface area, i.e., the area of contact between silicon and the electrolyte solution was 1.76 cm². A cathode was a platinum wire spiral. The spiral cathode ensures the most uniform current density distribution over the working area of the cell. To maintain the uniform acid concentration over the entire cell volume during etching, the Biosan OS-20 orbital mixer with the tunable rate of rotation was used. For better mixing, the vertical motion of the solution was created by blades placed in the cell.

A current with the modulated amplitude is applied to the electrochemical cell. The pore diameter monotonically depends
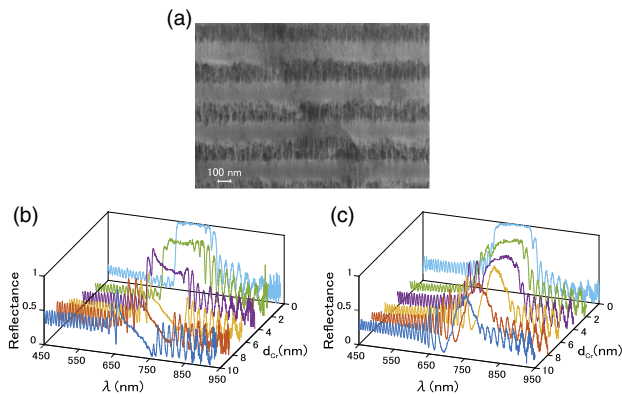
Fig. 6. (a) Scanning electron microscope image of the fabricated sample, reflectance spectra of the (b) LHL and (c) HLH structures at different chromium layer thicknesses.

Fig. 7. Measured transmittance spectra of (a) the LHL and (b) HLH structures at different chromium layer thicknesses.

on the etching current density and alternating large and small current pulses supplied to the cell ensure the formation of sequential layers with different porosities. To reduce the absorptance of the structure, porous silicon is thermally oxidized to porous quartz. The spectra were measured at normal incidence using a halogen light bulb as a light source and an Avesta ASP100M spectrometer as a detector.

The scanning electron microscope image of the fabricated sample is shown in Fig. 6(a). The reflectance spectra of the structures at different chromium layer thicknesses are presented in Figs. 6(b) and 6(c).

It can be seen that in the HLH configuration, the TPP does not form regardless of the chromium layer thickness. The increase in the d_{Cr} value leads to the bandgap narrowing and a decrease in the reflectance at its wavelengths. In the LHL structure, the situation is different. The gradual growth of the chromium layer thickness leads to the formation of the frequency range with the near-zero reflectance at the long-wavelength edge of the initial photonic bandgap. In the experiment, we failed to completely suppress reflection; it remained at a level of 5%. Nevertheless, the analytical, numerical, and experimental data are in good agreement.

This frequency range corresponds to the TPP localized at the Bragg reflector/chromium layer interface. It is worth noting that the TPP manifests itself in the reflectance spectra of only the samples with the chromium layer thicker than 4 nm. The use of thinner layers does not allow the desired reflectivity of the metallic mirror and, consequently, the localized state formation, to be obtained.

The measured transmittance spectra of the LHL and HLH structures at different chromium layer thicknesses are shown in Fig. 7. One can see that the passbands form neither in the LHL structure bandgap nor in the HLH one. Based on the energy conservation law ($A + R + T = 1$), we can conclude that 95% of the incident light at the TPP wavelength is only absorbed in the LHL structure. This means, in fact, the validity of conditions [Eqs. (5) and (11)].

The transition from one configuration to the other makes it possible to change the reflection regime and ensure the broadband absorption. However, in contrast to the calculation
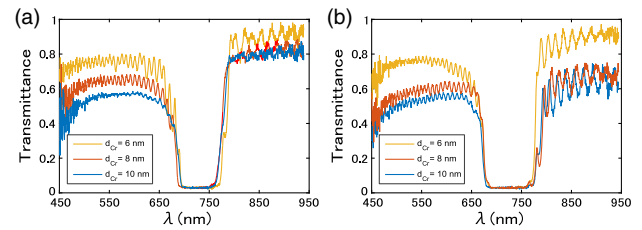
model, the TPP frequency does not lie at the bandgap center but is shifted to the long-wavelength edge (Fig. 6). The fact is that during deposition of chromium onto the BM, chromium particles inevitably hit pores of the BM first layer. As a result, a thin nanocomposite layer with the porous quartz matrix and chromium nanoparticles dispersed in it forms. The occurrence of the nanocomposite layer [46–48] causes the additional phase φ_{NC} of the incident wave and, consequently, to the TPP frequency shift to the long-wavelength region.

To check the effect of this factor, we numerically calculated the reflectance spectra of the structure with regard to the formation of the nanocomposite layer at the interface between chromium and the BM (Fig. 8). The effective permittivity of the nanocomposite is determined by the Maxwell–Garnet formula [49] widely used in studying matrix media [50], when a small volume fraction of isolated metal inclusions is dispersed in the matrix material.

Analysis of the results obtained showed that the account for the nanocomposite layer formation at the metallic layer/BM interface makes it possible to obtain the best agreement with the experimental data. This indicates that the effective medium and its parameters were chosen correctly. Thus, the minimum reflection is observed at a wavelength of $\lambda = 753.7$ nm. In this case the quality factor of the broadband TPP is $Q \approx 5$. It should be noted that this result has a good agreement with results of coupled mode theory (Fig. 2) since the broadest linewidth of TPP was obtained.
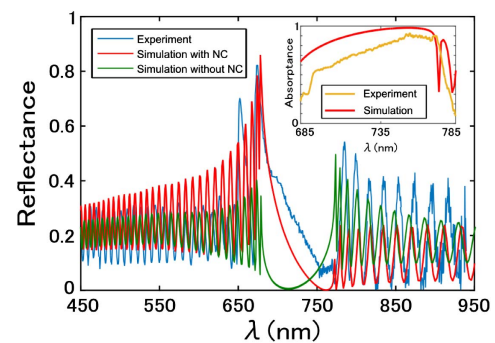

Fig. 8. Experimental and calculated reflectance spectra of the LHL structure with regard to the formation of the nanocomposite layer with a thickness of $d_{NC} = 20$ nm at the interface between the chromium and Bragg mirror. The nanocomposite filling factor is $f = 30\%$. The chromium layer thickness is $d_{Cr} = 6$ nm. The insert shows the calculated and experimental absorption spectra of the structure within the BM bandgap.
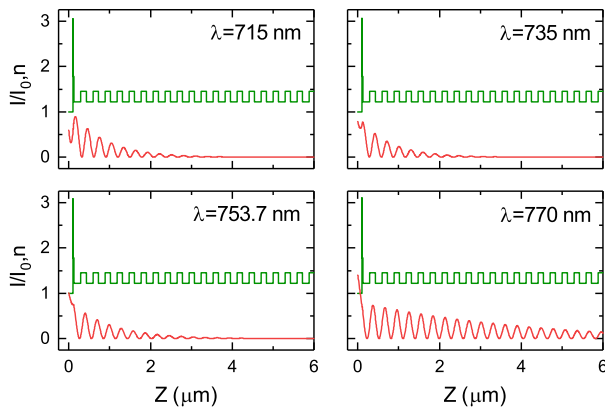
Fig. 9. Local field intensity distribution at the TPP wavelength and near to it normalized to the input intensity (red line) and spatial distribution of the refractive index of the PC layers (green line).

Experimental and calculated absorption spectra of the structure are shown in the inset of Fig. 8. Experimental absorption was determined by energy conservation law. The difference between the experimental data and the numerical calculation is due to the complexity of measuring the transmission and reflection spectra from the same point of the sample. It is important to note that the integrated absorptance of the structure in the range from 670 to 780 nm (inside the bandgap) is 81%, which is twice the absorptance of the chromium film in the same spectral range. Thus, excitation of broadband TPP is an effective technique to increase absorption in a certain spectral range.

The spatial distributions of the local field intensity at the TPP wavelength and near it are presented in Fig. 9. It is important to note that in the studied structure the field is better localized below the TPP wavelength. The shift of the maximal local field intensity from the TPP wavelength can be explained by the temporal coupled mode theory. According to this theory, the intensity of the localized field can be defined as (see Section 2.A)

$$|A|^2 = \frac{2\gamma_m |s_{1+}|^2}{-(\omega - \omega_0)^2 + (\gamma_m + \gamma_{bm} + \gamma_d)^2}. \quad (14)$$

From this equation it follows that the maximal field intensity at the TPP wavelength is observed in the case when $\omega = \omega_0$ and γ does not depend on the frequency. Otherwise, the frequency ω of maximal localization is determined by the calculation of the derivative $\partial |A| / \partial \omega$ with $\gamma_m(\omega), \gamma_{bm}(\omega), \gamma_d(\omega)$. The frequency ω is determined by $\partial |A| / \partial \omega = 0$ or

$$\frac{\partial \gamma_m}{\partial \omega} \left(\left(\sum \gamma_i \right)^2 - (\omega - \omega_0)^2 \right) - \cdots$$
$$- \gamma_m \left(-2(\omega - \omega_0) + 2 \sum \gamma_i \sum \frac{\partial \gamma_i}{\partial \omega} \right) = 0. \quad (15)$$

The BM has a finite length and the $\gamma_{bm} \neq 0$. Moreover, $\partial \gamma_{bm} / \partial \omega$ in the photonic bandgap is larger than $\partial \gamma_m / \partial \omega$ and $\partial \gamma_d / \partial \omega$. At a result, we have

$$\omega = \omega_0 + \frac{\partial \gamma_{bm}}{\partial \omega} \sum \gamma_i. \quad (16)$$

According to Eq. (1) γ_{bm} is proportional to the BM transmittance. Define γ_{bm} as

$$\gamma_{bm} = \exp \left[C \left(\frac{\omega - \omega_{Br}}{\Delta \omega} \right)^2 - 1 \right], \quad (17)$$

where ω_{Br} is the frequency of the center of the BM bandgap, C is the constant, and $\Delta \omega$ is the half-width of the photonic bandgap. For example, at the frequency $\omega = \omega_{Br}$ transmittance in the center of the BM bandgap is zero as a consequence $\gamma_{bm} = 0$. Offset from ω_{Br} leads to increasing the transmittance and γ_{bm}. From Eqs. (16) and (17) it follows that

$$\omega = \frac{\omega_0 - \omega_{Br} \gamma_{bm} \frac{2C}{\Delta \omega^2} \sum \gamma_i}{1 - \gamma_{bm} \frac{2C}{\Delta \omega^2} \sum \gamma_i}, \quad (18)$$

where $0 < \gamma_{bm} \frac{2C}{\Delta \omega^2} \sum \gamma_i < 1$. In our case $\omega_0 < \omega_{Br}$, and for different $\gamma_{bm} \frac{2C}{\Delta \omega^2} \sum \gamma_i$ in the range 0–1 the frequency ω is greater than ω_0. As a result, the maximum field intensity is observed at frequencies higher than the TPP frequency (or shorter wavelengths). This result has a good agreement with simulation by the transfer matrix method (see Fig. 9). Note also that the light field at the $\lambda = 715$ nm is localized in the region comparable with the wavelength.

3. CONCLUSIONS

We have predicted and observed the broadband Tamm plasmon polariton localized at the interface between the Bragg mirror and a thin metallic layer. The possibility of the localized state formation was predicted analytically and implemented experimentally. It was shown that the properties of the Tamm plasmon polariton can be predicted by the coupled mode theory and Cole–Cole phase diagrams. It is shown that the variation of the metal film material permits control of the width of the resonance line of the Tamm plasmon polariton. Moreover, it was found that the plasmonic materials can be grouped by the values of the relaxation rates in the conditions of the critical coupling of the Tamm plasmon polariton with the incident field. In particular, it was shown that the use of a metal film of chromium allows obtaining the maximum width of the spectral line. The described qualitative analytical approaches can be used to form the TPP structures with specified parameters, which is of great importance for application in plasmonics and optoelectronics.

REFERENCES

1. M. A. Kaliteevski, I. Iorsh, S. Brand, R. A. Abram, J. M. Chamberlain, A. V. Kavokin, and I. A. Shelykh, "Tamm plasmon-polaritons: possible electromagnetic states at the interface of a metal and a dielectric Bragg mirror," Phys. Rev. B **76**, 165415 (2007).
2. I. E. Tamm, "Tamm_t1_1975ru.pdf," Phys. Z. Sowjetunion **1**, 733 (1932).
3. M. E. Sasin, R. P. Seisyan, M. A. Kaliteevski, S. Brand, R. A. Abram, J. M. Chamberlain, A. Y. Egorov, A. P. Vasil'ev, V. S. Mikhrin, and A. V. Kavokin, "Tamm plasmon polaritons: slow and spatially compact light," Appl. Phys. Lett. **92**, 251112 (2008).

4. T. Goto, A. V. Dorofeenko, A. M. Merzlikin, A. V. Baryshev, A. P. Vinogradov, M. Inoue, A. A. Lisyansky, and A. B. Granovsky, "Optical Tamm states in one-dimensional magnetophotonic structures," Phys. Rev. Lett. **101**, 14–16 (2008).

5. S. Y. Vetrov, R. G. Bikbaev, and I. Timofeev, "Optical Tamm states at the interface between a photonic crystal and a nanocomposite with resonance dispersion," J. Exp. Theor. Phys. **117**, 988–998 (2013).

6. S. Y. Vetrov, R. G. Bikbaev, and I. Timofeev, "The optical Tamm states at the edges of a photonic crystal bounded by one or two layers of a strongly anisotropic nanocomposite," Opt. Commun. **395**, 275–281 (2017).

7. S. Y. Vetrov, P. S. Pankin, and I. Timofeev, "The optical Tamm states at the interface between a photonic crystal and a nanocomposite containing core-shell particles," J. Opt. **18**, 065106 (2016).

8. R. G. Bikbaev, S. Y. Vetrov, and I. Timofeev, "The optical Tamm states at the interface between a photonic crystal and nanoporous silver," J. Opt. **19**, 015104 (2017).

9. R. G. Bikbaev, S. Y. Vetrov, and I. Timofeev, "Optical Tamm states at the interface between a photonic crystal and a gyroid layer," J. Opt. Soc. Am. B **34**, 2198–2202 (2017).

10. S. Y. Vetrov, R. G. Bikbaev, N. V. Rudakova, K.-P. Chen, and I. V. Timofeev, "Optical Tamm states at the interface between a photonic crystal and an epsilon-near-zero nanocomposite," J. Opt. **19**, 085103 (2017).

11. R. G. Bikbaev, S. Y. Vetrov, and I. V. Timofeev, "Two types of localized states in a photonic crystal bounded by an epsilon near zero nanocomposite," Photonics **5**, 22 (2018).

12. R. G. Bikbaev, S. Y. Vetrov, and I. V. Timofeev, "Epsilon-near-zero absorber by tamm plasmon polariton," Photonics **6**, 28 (2019).

13. Y. Gong, X. Liu, L. Wang, H. Lu, and G. Wang, "Multiple responses of TPP-assisted near-perfect absorption in metal/Fibonacci quasiperiodic photonic crystal," Opt. Express **19**, 9759–9769 (2011).

14. Y. Gong, X. Liu, H. Lu, L. Wang, and G. Wang, "Perfect absorber supported by optical Tamm states in plasmonic waveguide," Opt. Express **19**, 18393–18398 (2011).

15. M. Fang, F. Shi, and Y. Chen, "Unidirectional all-optical absorption switch based on optical Tamm state in nonlinear plasmonic waveguide," Plasmonics **11**, 197–203 (2016).

16. C.-H. Xue, F. Wu, H.-T. Jiang, Y. Li, Y.-W. Zhang, and H. Chen, "Wide-angle spectrally selective perfect absorber by utilizing dispersionless Tamm plasmon polaritons," Sci. Rep. **6**, 39418 (2016).

17. W. Zhang and S. Yu, "Bistable switching using an optical Tamm cavity with a Kerr medium," Opt. Commun. **283**, 2622–2626 (2010).

18. X.-L. Zhang, J.-F. Song, X.-B. Li, J. Feng, and H.-B. Sun, "Optical Tamm states enhanced broad-band absorption of organic solar cells," Appl. Phys. Lett. **101**, 243901 (2012).

19. Z.-Y. Yang, S. Ishii, T. Yokoyama, T. D. Dao, M.-G. Sun, P. S. Pankin, I. Timofeev, T. Nagao, and K.-P. Chen, "Narrowband wavelength selective thermal emitters by confined Tamm plasmon polaritons," ACS Photonics **4**, 2212–2219 (2017).

20. S.-G. Huang, K.-P. Chen, and S.-C. Jeng, "Phase sensitive sensor on Tamm plasmon devices," Opt. Mater. Express **7**, 1267–1273 (2017).

21. B. Auguié, M. C. Fuertes, P. C. Angelomé, N. L. Abdala, G. J. A. A. Soler Illia, and A. Fainstein, "Tamm plasmon resonance in mesoporous multilayers: toward a sensing application," ACS Photonics **1**, 775–780 (2014).

22. A. R. Gubaydullin, C. Symonds, J. Bellessa, K. A. Ivanov, E. D. Kolykhalova, M. E. Sasin, A. Lemaitre, P. Senellart, G. Pozina, and M. A. Kaliteevski, "Enhancement of spontaneous emission in Tamm plasmon structures," Sci. Rep. **7**, 9014 (2017).

23. A. P. Vinogradov, A. V. Dorofeenko, S. G. Erokhin, M. Inoue, A. A. Lisyansky, A. M. Merzlikin, and A. B. Granovsky, "Surface state peculiarities in one-dimensional photonic crystal interfaces," Phys. Rev. B **74**, 045128 (2006).

24. C.-H. Xue, H.-T. Jiang, H. Lu, G.-Q. Du, and H. Chen, "Efficient third-harmonic generation based on Tamm plasmon polaritons," Opt. Lett. **38**, 959–961 (2013).

25. B. I. Afinogenov, V. O. Bessonov, and A. A. Fedyanin, "Second-harmonic generation enhancement in the presence of Tamm plasmon-polaritons," Opt. Lett. **39**, 6895–6898 (2014).

26. I. V. Treshin, V. V. Klimov, P. N. Melentiev, and V. I. Balykin, "Optical Tamm state and extraordinary light transmission through a nanoaperture," Phys. Rev. A **88**, 023832 (2013).

27. C. Symonds, G. Lheureux, J. P. Hugonin, J. J. Greffet, J. Laverdant, G. Brucoli, A. Lemaitre, P. Senellart, and J. Bellessa, "Confined Tamm plasmon lasers," Nano Lett. **13**, 3179–3184 (2013).

28. C. Symonds, A. Lemaître, P. Senellart, M. H. Jomaa, S. Aberra Guebrou, E. Homeyer, G. Brucoli, and J. Bellessa, "Lasing in a hybrid GaAs/silver Tamm structure," Appl. Phys. Lett. **100**, 121122 (2012).

29. O. Gazzano, S. Michaelis de Vasconcellos, K. Gauthron, C. Symonds, P. Voisin, J. Bellessa, A. Lemaître, and P. Senellart, "Single photon source using confined Tamm plasmon modes," Appl. Phys. Lett. **100**, 232111 (2012).

30. J. Gessler, V. Baumann, M. Emmerling, M. Amthor, K. Winkler, S. Höfling, C. Schneider, and M. Kamp, "Electro optical tuning of Tamm-plasmon exciton-polaritons," Appl. Phys. Lett. **105**, 181107 (2014).

31. X.-L. Zhang, J. Feng, X.-C. Han, Y.-F. Liu, Q.-D. Chen, J.-F. Song, and H.-B. Sun, "Hybrid Tamm plasmon-polariton/microcavity modes for white top-emitting organic light-emitting devices," Optica **2**, 579–584 (2015).

32. C.-Y. Chang, Y.-H. Chen, Y.-L. Tsai, H.-C. Kuo, and K.-P. Chen, "Tunability and optimization of coupling efficiency in Tamm plasmon modes," IEEE J. Sel. Top. Quantum Electron. **21**, 262–267 (2015).

33. J. D. Joannopoulos, S. G. Johnson, J. N. Winn, and R. D. Meade, *Photonic Crystals: Molding the Flow of Light*, 2nd ed. (2008).

34. H. A. Haus, *Waves and Fields in Optoelectronics* (Prentice Hall, 1983).

35. B. Auguié, A. Bruchhausen, and A. Fainstein, "Critical coupling to Tamm plasmons," J. Opt. **17**, 035003 (2015).

36. M. Born and E. Wolf, *Principles of Optics*, 7th ed. (Cambridge University, 1999).

37. P. Johnson and R. W. Christy, "Optical constants of the noble metals," Phys. Rev. B **6**, 4370–4379 (1972).

38. M. A. Ordal, R. J. Bell, R. W. Alexander, L. A. Newquist, and M. R. Querry, "Optical properties of Al, Fe, Ti, Ta, W, and Mo at submillimeter wavelengths," Appl. Opt. **27**, 1203–1209 (1988).

39. W. S. M. Werner, K. Glantschnig, and C. Ambrosch-Draxl, "Optical constants and inelastic electron-scattering data for 17 elemental metals," J. Phys. Chem. Ref. Data **38**, 1013–1092 (2009).

40. A. D. Rakić, "Algorithm for the determination of intrinsic optical constants of metal films: application to aluminum," Appl. Opt. **34**, 4755–4767 (1995).

41. P. Johnson and R. Christy, "Optical constants of transition metals: Ti, V, Cr, Mn, Fe, Co, Ni, and Pd," Phys. Rev. B **9**, 5056–5070 (1974).

42. K. S. Cole and R. H. Cole, "Dispersion and absorption in dielectrics I. Alternating current characteristics," J. Chem. Phys. **9**, 341–351 (1941).

43. A. Y. P. Yeh, *Optical Waves in Crystals: Propagation and Control of Laser Radiation*, Wiley Series in Pure and Applied Optics (Wiley, 1984).

44. P. Yeh, "Electromagnetic propagation in birefringent layered media," J. Opt. Soc. Am. **69**, 742–756 (1979).

45. S. E. Svyakhovskiy, A. I. Maydykovsky, and T. V. Murzina, "Mesoporous silicon photonic structures with thousands of periods," J. Appl. Phys. **112**, 013106 (2012).

46. S. Y. Vetrov, A. Y. Avdeeva, R. G. Bikbaev, and I. Timofeev, "Traveling of light through a 1D photonic crystal containing a defect layer with resonant dispersion," Opt. Spectrosc. **113**, 517–521 (2012).

47. S. G. Moiseev, V. A. Ostatochnikov, and D. I. Sementsov, "Defect mode suppression in a photonic crystal structure with a resonance nanocomposite layer," Quantum Electron. **42**, 557–560 (2012).

48. E. Pedrueza, J. L. Valdés, V. Chirvony, R. Abargues, J. Hernández-Saz, M. Herrera, S. I. Molina, and J. P. Martínez-Pastor, "Novel method of preparation of gold-nanoparticle-doped TiO2 and SiO2 plasmonic thin films: optical characterization and comparison with Maxwell-Garnett modeling," Adv. Funct. Mater. **21**, 3502–3507 (2011).

49. J. C. M. Garnett, "Colours in metal glasses and in metallic films," Philos. Trans. R. Soc. London A **203**, 385–420 (1904).

50. A. Sihvola, *Electromagnetic Mixing Formulas and Applications* (IET, 1999).